Annals of Biomedical Engineering, Vol. 31, pp. 548–563, 2003
Printed in the USA. All rights reserved.

0090-6964/2003/31(5)/548/16/$20.00

Voronoi Polyhedra Analysis of Optimized Arterial Tree Models

RUDOLF KARCH,[1] FRIEDERIKE NEUMANN,[1] MARTIN NEUMANN,[2] PAUL SZAWLOWSKI,[1] and WOLFGANG SCHREINER[1]

[1]Department of Medical Computer Sciences, University of Vienna, Spitalgasse 23, A-1090 Wien, Austria and [2]Institute of Experimental Physics, Section for Computational Physics, University of Vienna, Strudlhofgasse 4, A-1090 Wien, Austria

(Received 7 June 2001; accepted 4 February 2003)

Abstract—Topological and metric properties of Voronoi polyhedra (VP) generated by the distal end points of terminal segments in arterial tree models grown by the method of constrained constructive optimization (CCO) are analyzed with the aim to characterize the spatial distribution of their supply sites relative to randomly distributed points as a reference model. The distributions of the number N_f of Voronoi cell faces, cell volume V, surface area S, area A of individual cell faces, and asphericity parameter α of the CCO models are all significantly different from the ones of random points, whereas the distributions of V, S, and α are also significantly different among CCO models optimized for minimum intravascular volume and minimum segment length ($p<0.0001$). The distributions of N_f, V, and S of the CCO models are reasonably well approximated by two-parameter gamma distributions. We study scaling of intravascular blood volume and arterial cross-sectional area with the volume of supplied tissue, the latter being represented by the VP of the respective terminal segments. We observe scaling exponents from 1.20 ± 0.007 to 1.08 ± 0.005 for intravascular blood volume and 0.77 ± 0.01 for arterial cross-sectional area. Setting terminal flows proportional to the associated VP volumes during tree construction yields a relative dispersion of terminal flows of 37% and a coefficient of skewness of 1.12. © *2003 Biomedical Engineering Society.* [DOI: 10.1114/1.1566444]

Keywords—Voronoi cell, Gamma distribution, Lognormal distribution, Scaling, Blood flow, Relative dispersion, Computer simulation.

INTRODUCTION

Arterial trees serving an organ fulfill the basic physiological task to deliver blood to and remove metabolic end products from the tissue they supply. During the last decades arterial trees have been the subject of numerous modeling studies, ranging from self-similar fractal approaches[15,56] and anatomically derived branching tube models[7,28,55] to combined geometric and functional vascular growth models.[18,32,47] Still another approach is taken by the method of constrained constructive optimization (CCO).[48,49] Based on the hypothesis of optimal design,[45] CCO allows to generate arterial tree models of some 10^4 vessel segments from a feeding artery down to small arteries without directly using anatomical data. Despite the numerous simplifying assumptions inherent in this model, CCO trees exhibit a realistic visual appearance and quite satisfactorily reproduce various properties of real arterial trees, such as branching angle statistics,[50] diameter ratios of parent and daughter segments, and the volume of the large arteries.[26]

Concerning the relationship between structure and function of arterial trees serving an organ, one important characteristic of a tree model is the spatial distribution of its terminal blood supply points.[32] The characterization of spatial structures is a challenging issue,[16] and various approaches have been suggested in the literature, including nearest-neighbor distance methods,[44] second-order analysis (pair correlation function),[52] and fractal descriptions.[29] In this paper, we consider the terminal locations of CCO trees as a point pattern and apply the method of Voronoi analysis to characterize its spatial distribution.

The Voronoi polyhedron associated with a central (generating) point P is defined as the convex region of space closer to P than to any other point P' of a given set of points. The Voronoi tessellation of a set of distinct points leads to a partition of space into convex nonoverlapping polyhedra that completely fill the space. Voronoi tessellations originally emerged in the context of a number-theoretical problem[12,58] and have since then been successfully applied as a model in such diverse fields of science as physics (liquid structure,[37,43] crystal growth),[35] biology (cellular patterns),[20] and medicine (capillary domains).[21] In particular, Kurz and Sandau[32] have proposed the assessment of the end-point distribution as an important characteristic of vascular trees and used Voronoi tessellations to describe the apparent end-point distribution of arteries in the chorioallantoic membrane of chicken eggs.

Here, we are interested in various topological and metric properties of the Voronoi polyhedra (VP) associ-

Address correspondence to Rudolf Karch, University of Vienna, Department of Medical Computer Sciences, Spitalgasse 23, A-1090 Wien, Austria. Electronic mail: rudolf.karch@univie.ac.at

ated with the distal end points of terminal segments of CCO trees. Since Voronoi tessellations generated by purely randomly distributed points in two- and three-dimensional space (so-called Poisson–Voronoi tessellations) have been extensively studied in the literature,[19,30,31,35] we use this model as a reference. In particular, we address the question how different modes of tree optimization affect the shape of the resulting VP. As an application, the Voronoi tessellations are used to assign the region of supplied tissue to each terminal segment in a quite natural and unambiguous way. For comparison of model predictions with experimental data we consider scaling relations between intravascular blood volume and arterial cross-sectional area with the volume of supplied tissue. In a further application, we present a modification of the algorithm of CCO, namely to set terminal flows proportional to the associated VP volumes during tree generation.

This paper is organized as follows: In the next section we briefly summarize the method of CCO and the algorithm used for the construction of Voronoi tessellations and describe the quantities calculated from the VP. In the following sections we present and discuss the results obtained and summarize the conclusions drawn.

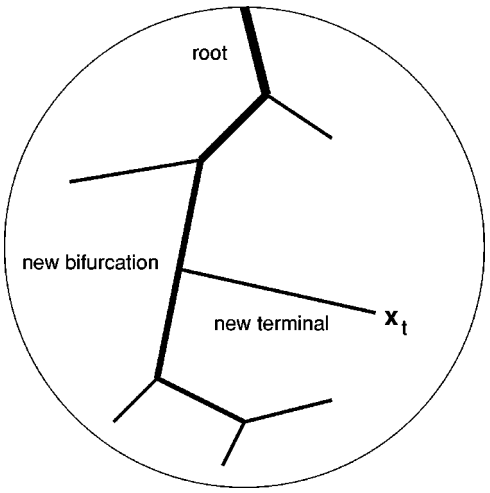

FIGURE 1. Schematic representation of the growth of a CCO tree. A new terminal positon x_t is selected at random within a circular perfusion area and connected to an existing tree segment, thus forming a new terminal segment and a new bifurcation. In the next step, the geometry of the new bifurcation is optimized with respect to a given target function *T*, Eq. (2), and prescribed boundary conditions for pressures and flows.

METHODS

The Algorithm of Tree Generation

CCO trees, originally introduced in a two-dimensional framework,[48,49] constitute some kind of synthesis between rule-based fractal approaches and models directly derived from the anatomy of real arterial trees: CCO employs the principle of optimal design,[45] which has long been hypothesized in the literature to hold for single bifurcations of arterial trees.[36,62] In an ''*ab initio*'' like fashion, CCO trees are constructed from a single root segment by subsequently adding new terminal segments from randomly chosen positions within the geometric model of the perfusion area, until a given number of terminal segments N_{term} is reached (Fig. 1). At each step of growth, the geometry of the new bifurcation is optimized under prescribed physiological boundary conditions. This procedure allows to generate computer models of arterial trees with an ''arbitrary'' number of segments, limited only by the computer resources available. One of the main advantages of CCO trees is the fact that at each step of construction we have at hand the complete geometric data set of the tree, including segment locations and diameters. It should be noted, however, that no attempt is made to model the actual growth process of real arterial trees.[22]

For ease of reference, we summarize the main points of the method of CCO:[25,49] Arterial trees are represented as binary branching trees, vessel segments are modeled by rigid cylindrical tubes, and the precise geometry of bifurcations is not considered. Blood is assumed an incompressible, homogeneous Newtonian fluid and the hydrodynamic resistance of individual segments is estimated by means of Poiseuille's law.[13] Optimization of single bifurcations is performed under the following set of boundary conditions: At each bifurcation, the diameters of the parent segment (d_0) and the doughter segments (d_1, d_2) obey a power law of the form

$$d_0^\gamma = d_1^\gamma + d_2^\gamma \tag{1}$$

with a constant exponent $\gamma > 0$. At a given total perfusion flow Q_{perf}, individual terminal flows $Q_{\text{term},i}$ with $\Sigma Q_{\text{term},i} = Q_{\text{perf}}$, and at a given diameter of the root segment, all remaining segment diameters are scaled so as to fulfill Eq. (1) at each bifurcation and to maintain the prescribed flows. The position of each new bifurcation is calculated so as to minimize the quantity

$$T = \sum_i l_i d_i^\lambda , \tag{2}$$

where l_i is the length of segment i and λ is a free parameter: $\lambda = 2$ minimizes total intravascular volume,[24] whereas $\lambda = 0$ minimizes total segment length.

As of particular interest for the present work, we note that the coordinates of new terminal positions $\mathbf{x}_t$ are drawn from a random number sequence with a uniform distribution. In particular, $\mathbf{x}_t$ is accepted as a new terminal site only if it is not too close to the segments of the

tree grown thus far. This ''repulsion criterion'' acts like a step potential of infinite height in the neighborhood of each segment: Terminal positions $\mathbf{x}_t$ within the potential well are rejected, all others remain unaffected. As a result, the terminal positions of CCO trees no longer represent a sample from a uniform distribution in space, and it is one goal of the present paper to characterize the differences.

The Construction of Voronoi Polyhedra

The efficient construction of the Voronoi tessellation of a set of points, in particular in three-dimensional space, is a nontrivial task and much effort has been put into the development of such algorithms in the field of computational geometry.[3,39,40] In this paper, we have used the Qhull software package,[4] which implements the Quickhull algorithm[40] to construct the Voronoi tessellation of a given set of input points. The Qhull program utilizes the following relation between convex hulls (i.e., the smallest convex set that contains a given set of points) and Voronoi tessellations:[5,9] To obtain for a given set of points in $\mathbf{R}^2$ the Delaunay triangulation (i.e., the straight-line dual of the Voronoi tessellation of these points),[40] the points are lifted to a paraboloid in $\mathbf{R}^3$ and the convex hull of these transformed points is computed in $\mathbf{R}^3$; the set of edges of the lower convex hull (i.e., that part of the hull which is visible from the xy plane)[3] is the Delaunay triangulation of the original points. This algorithm can immediately be generalized to higher dimensions. Since the Delaunay tessellation is the dual of the Voronoi tessellation, the problem of constructing a m-dimensional Voronoi diagram is thus reduced to a convex hull problem in $(m+1)$ dimensions.

The data structure produced by Qhull includes the vertex coordinates of the Voronoi polygon-edges in two-dimensional (2D) space and polyhedra-faces in three-dimensional (3D) space for all pairs of adjacent input sites; from this information we readily obtain the desired topological (e.g., number of faces) and metric (e.g., volume, surface area) properties of the VP. Since Qhull uses floating point arithmetic, the results are only approximate. As a necessary condition for the consistency of the tessellations, the sum of the VP volumes must be equal to the total volume of the system. We therefore calculated the respective sum and compared it with the perfusion volume of the tree. We always found a difference not larger than approximately $10^{-7}\%$.

Calculated Quantities

The topology of a Voronoi polyhedron is completely characterized by the number of vertices N_v, the number of edges N_e, and the number of faces N_f. These three parameters are related by two topological constraints, namely the classical Euler formula[40]

$$N_v - N_e + N_f = 2 \tag{3}$$

and

$$3N_v = 2N_e . \tag{4}$$

The last equation follows, if we assume that the generating points are in general position,[39] so that every vertex shares exactly three faces (and thus edges) and every edge connects exactly two vertices.[23,46] (This assumption is reasonable for CCO trees, since it is extremely unlikely for random systems that four or more points lie on the same plane and five or more points lie on the boundary of a sphere.) Hence, only one of the previous parameters is independent. Here, we have used N_f as the independent quantity to describe the topology of the VP. For the remaining two parameters we then have $N_v = 2N_f - 4$ and $N_e = 3N_f - 6$.

In addition to the topological quantities, we have evaluated the following metric quantities of the Voronoi polyhedra: The area A_k of the individual faces

$$A_k = \frac{1}{2} \sum_{j=2}^{n_v^{(k)}-1} \left| (\mathbf{r}_j^{(k)} - \mathbf{r}_1^{(k)}) \times (\mathbf{r}_{j+1}^{(k)} - \mathbf{r}_1^{(k)}) \right|, \tag{5}$$

where $n_v^{(k)}$ is the number of vertices of the kth face and $\mathbf{r}_j^{(k)}$ is the position vector of the jth vertex of this face; the total surface area S:

$$S = \sum_{k=1}^{N_f} A_k , \tag{6}$$

and the total volume V:

$$V = \frac{1}{3} \sum_{k=1}^{N_f} h_k A_k , \tag{7}$$

where h_k denotes the normal distance of the center of the Voronoi polyhedron from its kth face. By definition of a Voronoi tessellation, each face of a cell is part of the perpendicular bisector of the line segment between the cell center and one of its N_f nearest neighbors. Therefore, the kth face exactly divides the distance r_k between the center and the corresponding nearest neighbor into two equal parts, and we have $h_k = r_k/2$.

Following Ruocco *et al.*,[46] we have also calculated the asphericity parameter α:

$$\alpha = \frac{S^3}{36\pi V^2}, \tag{8}$$

TABLE 1. Simulation parameters.

Parameter	Meaning	Value	Reference
p_{perf}	Perfusion pressure	100 mm Hg	10
Q_{perf}	Perfusion flow	500 ml/min	11
η	Viscosity of blood	3.6 cp	34
r_{root}	Radius of the root segment	2 mm	27
γ	Bifurcation exponent	2.55	2
N_{term}	Number of terminals	6000	
V_{perf}	Volume of perfusion area	100 cm^3	

which measures the deviation of the shape of a polyhedron from that of a perfect sphere. By definition, α equals 1 for a sphere, and larger values of α indicate a more aspheric polyhedron, e.g., $\alpha = 1.91$ for a cube.

RESULTS

Generation of Model Trees

We have generated ten model trees for each value of the optimization parameter $\lambda = 0$ and $\lambda = 2$. The model realizations were obtained by means of different seeds of the random number sequences for tossing new terminal locations; all remaining model parameters were left unchanged for the set of ten trees within each series. The trees were generated in a cubic slab of 4.642 cm side length. Simulation parameters are listed in Table 1. These parameters were chosen so as to model the large arteries of the coronary arterial tree supplying approximately 100 g of myocardial tissue.[26] Figure 2 shows a specific realization for each of the generated models. As can be seen, trees optimized for minimum segment length ($\lambda = 0$) exhibit a strongly meandering structure. Although the case $\lambda = 0$ is not exceedingly realistic, we have included this model in order to study if and how such a structure is reflected in the topological and metric properties of the corresponding VP.

As a reference model for the spatial arrangement of terminal end-points in CCO trees, we have generated in the same geometry (cubic slab) ten samples of purely random points drawn from a uniform distribution, i.e., realizations of a so-called Poisson point process.[39] The number N of random points was chosen the same as the number N_{term} of terminals in the respective tree models.

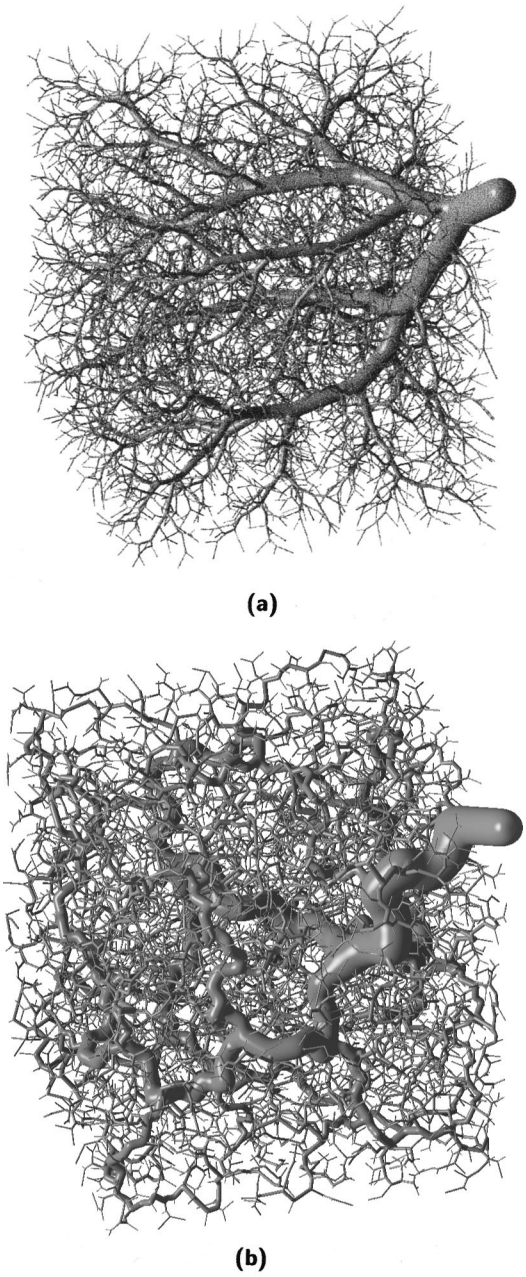

FIGURE 2. Visual representation of CCO trees optimized for minimum intravascular volume (a) and minimum total segment length (b). Simulation parameters are given in Table 1. Visualization was performed by representing the vessel segments as the isosurface of a pseudopotential assigned to the whole tree (see Neumann *et al.*, Ref. 38).

Construction of Voronoi Polyhedra

In the present paper we are concerned with tree structures grown in a bounded region of space. To calculate the Voronoi tessellations of such regions with the distal end points of terminal segments as generator points we mirror these points along the boundaries and perform the Voronoi decomposition on the extended point set thus obtained. Finally, we keep only those polyhedra which are associated with the original point set. This procedure guarantees that the region boundaries are exactly recovered as parts of the calculated VP. Figure 3 illustrates the resulting tessellations for a 2D [panel (a)] and 3D [panel (b)] CCO tree with $N_{term} = 200$ and $N_{term} = 100$ terminal segments, respectively. In Fig. 3(a) we immediatly recognize a distinctive feature of CCO trees, namely that

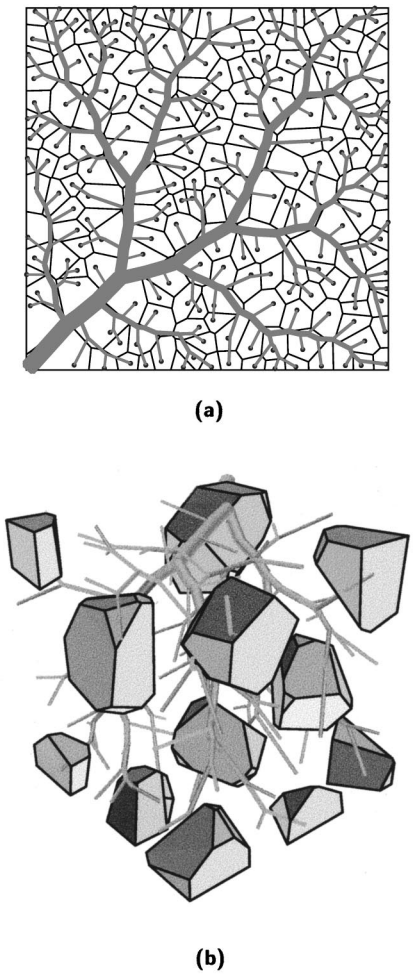

FIGURE 3. Voronoi tessellations generated by two- and three-dimensional CCO trees. (a) Voronoi polygons associated with the terminal end points of a 2D tree with $N_{term}=200$ terminal segments. (b) Selected Voronoi polyhedra as generated by the 3D tree of Fig. 2(a) with $N_{term}=100$ terminal segments. The graphical representation in panel (b) was obtained by means of the Geomview program (Ref. 33).

the larger Voronoi cells are always accompanied by the main vessels of the tree, whereas the relatively smaller cells are found in between.

Table 2 shows the results for the distributions of the topological and metric quantities evaluated. These results are based on ten realizations of each of the indicated models. The corresponding probability distributions are displayed in Figs. 4–7. For statistical testing of differences between these probability distributions Kolmogorov–Smirnov tests were performed on the level of significance of 0.0001.

Distribution of the Number of VP Faces

Figure 4 shows the distribution of the number of cell faces N_f for the CCO models. The distributions of N_f for CCO trees appear somewhat sharper, more symmetric

TABLE 2. Distribution of topological and metric quantities. $\langle X\rangle$, σ_X, γ_X, X_{min}, X_{max} are mean value, standard deviation, skewness, minimum, and maximum of the quantity X (number of cell faces N_f, cell volume V, surface area S, area of individual cell faces A, asphericity parameter α).

		$\lambda=2$	$\lambda=0$	Random
$\langle N_f\rangle$		14.13	14.19	14.58
σ_{N_f}		3.06	2.88	3.43
γ_{N_f}		0.27	0.16	0.33
$(N_f)_{min}$		5.00	5.00	5.00
$(N_f)_{max}$		28.00	28.00	31.00
$\langle V\rangle$	(cm^3)	0.0167	0.0167	0.0167
σ_V	(cm^3)	0.0062	0.0055	0.0074
γ_V		1.1882	1.4272	0.8410
V_{min}	(cm^3)	0.0020	0.0021	0.0006
V_{max}	(cm^3)	0.0664	0.0782	0.0716
$\langle S\rangle$	(cm^2)	0.3736	0.3734	0.3850
σ_S	(cm^2)	0.0850	0.0743	0.1030
γ_S		1.1882	1.1414	0.3898
S_{min}	(cm^2)	0.1104	0.1156	0.0581
S_{max}	(cm^2)	0.9156	1.0347	0.9588
$\langle A\rangle$	(cm^2)	0.0264	0.0263	0.0264
σ_A	(cm^2)	0.0234	0.0230	0.0269
γ_A		1.0690	1.0304	1.4810
A_{min}	(cm^2)	1×10^{-12}	1×10^{-12}	5×10^{-12}
A_{max}	(cm^2)	0.2656	0.3211	0.2754
$\langle\alpha\rangle$		1.7770	1.7540	2.0340
σ_α		0.2760	0.2771	0.4806
γ_α		1.8661	2.0624	2.9569
α_{min}		1.2881	1.2874	1.2987
α_{max}		5.0399	4.7639	13.1809

and have a mean value which is slightly shifted to the left compared with the one of random points (see σ_{N_f}, γ_{N_f}, and $\langle N_f\rangle$ in Table 2). Moreover, the N_f distributions of the CCO trees are significantly different from the

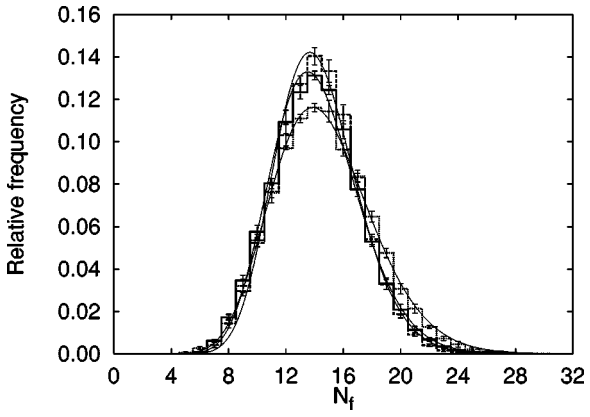

FIGURE 4. Normalized histogram of the number of cell faces N_f of the Voronoi polyhedra generated by CCO trees ($\lambda=2$: solid line; $\lambda=0$: dashed line) and by random points (dotted line). Error bars indicate mean±SD for ten realizations of each model. The continuous lines show the best-fit (discretized) two-parameter gamma distributions, Eqs. (9)–(10). See Table 3 for the parameter values.

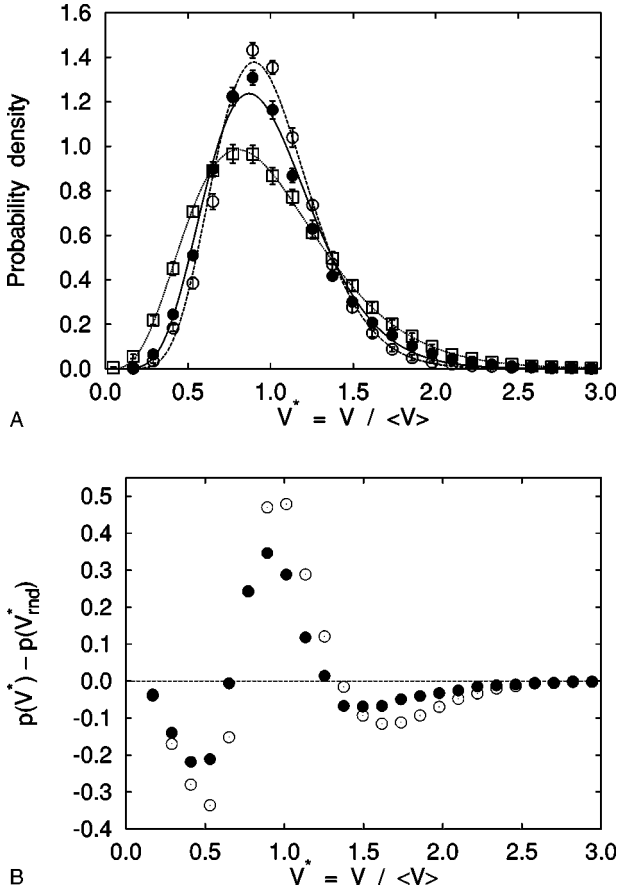

FIGURE 5. (a) Probability density distribution (mean±SD) of the normalized cell volume $V^*=V/\langle V\rangle$ of the Voronoi polyhedra generated by CCO trees ($\lambda=2$: solid circles; $\lambda=0$: open circles) and by random points (open squares). The continuous lines show the corresponding best-fit two-parameter gamma distributions ($\lambda=2$: solid line; $\lambda=0$: dashed line; random points: dotted line), Eq. (10). See Table 3 for the parameter values. (b) Distribution of normalized cell volumes V^* of CCO trees relative to the result $p(V^*_{rnd})$ for random points.

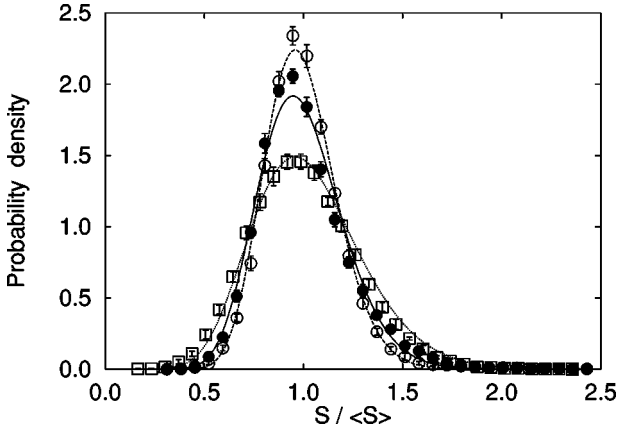

FIGURE 6. Probability density distribution (mean±SD) of the normalized total surface area $S^*=S/\langle S\rangle$ of the Voronoi polyhedra generated by CCO trees ($\lambda=2$: solid circles; $\lambda=0$: open circles) and by random points (open squares). The continuous lines show the corresponding best-fit two-parameter gamma distributions ($\lambda=2$: solid line; $\lambda=0$: dashed line; random points: dotted line), Eq. (10).

random points (two-sample Kolmogorov–Smirnov test, $p<0.0001$), whereas there is no significant difference between the tree models with $\lambda=2$ and $\lambda=0$ at the 0.0001 level of statistical significance.

Kumar *et al.*[30] suggested a discretized two-parameter gamma distribution

$$f(N_f)=\int_{N_f-1/2}^{N_f+1/2} p(x)\,dx \tag{9}$$

to approximate the distribution of cell faces in a 3D Poisson–Voronoi tessellation, where

$$p(x)=\frac{x^{a-1}}{b^a\Gamma(a)}\exp\left(-\frac{x}{b}\right),\quad x>0, \tag{10}$$

is the probability density function of the (continuous) two-parameter gamma distribution. $\Gamma(a)$ denotes the gamma function and the mean and variance of the distribution in Eq. (10) are given by ab and ab^2, respectively.

We have fitted the above distribution, Eq. (9), to our data, both for random points and for CCO models. The results for the best-fit parameters a and b together with the mean and standard deviation of the fitted gamma distribution are listed in Table 3. Comparing the values for the mean and standard deviation with the corresponding results of the original data (Table 2), we conclude that a two-parameter gamma distribution represents a good approximation to the distribution of cell faces, not

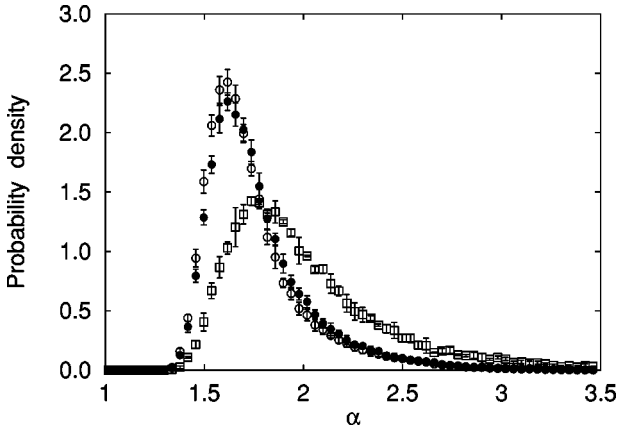

FIGURE 7. Probability density distribution (mean±SD) of the asphericity parameter α, Eq. (8). Solid circles: CCO trees with $\lambda=2$. Open circles: CCO trees with $\lambda=0$. Open squares: Poisson point process.

TABLE 3. Parameters of best-fit two-parameter gamma distributions. Entries for each variable (number of faces N_f, normalized volume $V^*=V/\langle V\rangle$ and surface area $S^*=S/\langle S\rangle$) denote the estimated parameter values for a and b (including the 68.3% confidence interval) as well as the mean ab and standard deviation $\sqrt{ab^2}$ of the respective best-fit gamma distribution, see Eq. (10).

	$\lambda=2$	$\lambda=0$	Random
N_f	21.43±0.51	24.89±0.82	17.46±0.35
	0.66±0.02	0.57±0.02	0.84±0.02
	14.17	14.24	14.71
	3.06	2.85	3.52
V^*	8.4489±0.2998	10.8246±0.3618	5.1062±0.0485
	0.1169±0.0043	0.0916±0.0031	0.1960±0.0018
	0.9876	0.9914	1.0007
	0.3398	0.3013	0.4429
S^*	21.8743±0.8567	30.0819±1.0022	13.9321±0.2737
	0.0454±0.0018	0.0329±0.0011	0.0741±0.0014
	0.9927	0.9907	1.0319
	0.2123	0.1806	0.2765

only for random points, but also for CCO trees (see also Fig. 4). Moreover, the moments of the N_f distribution (Table 2) reflect the differences in the spatial arrangement of the corresponding generating points, in particular between random points and terminal locations in CCO trees.

Distribution of Cell Volumes

Figure 5(a) shows the distributions of the reduced cell volumes, $V^*=V/\langle V\rangle$, for the CCO models studied. The cell volume distributions $p(V^*)$ of the tree models appear markedly different from the respective distribution of the Poisson–Voronoi tessellation, in particular with respect to their spread around the mean (see σ_V in Table 2): tree models are more sharply peaked around $\langle V^*\rangle=1$, and this behavior is even more pronounced for trees with $\lambda=0$ than for threes with $\lambda=2$. (Note that for the mean value we have $\langle V^*\rangle=1$ for each model. This is because we use a simulation box of fixed geometry and we keep the number of the generating points constant, so that the mean cell volume always takes the value $\langle V\rangle=V_{\mathrm{box}}/N$, and therefore $\langle V^*\rangle=1$, independent of the specific model.) The $p(V^*)$ distributions are significantly different between CCO models with $\lambda=2$ and $\lambda=0$ and between CCO models and random points (Kolmogorov–Smirnov test, $p<0.0001$).

The cell volume distribution of the random points is well approximated by a two-parameter gamma distribution, Eq. (10).[30] The best-fit parameter values for a and b are listed in Table 3. These values are consistent and in reasonable agreement with previous studies for Poisson–Voronoi tessellations.[30] Deviations in a and b are due to boundary effects. Fitting two-parameter gamma distributions to the $p(V^*)$ values of the tree models (see Table 3 for the estimated parameters) also yields a good approximation for these data, in particular along the left and the right tails; small differences can be observed only near the peaks of the distributions, see Fig. 5(a).

To further evaluate the features of $p(V^*)$ for CCO trees, we have plotted the differences between $p(V^*)$ of the tree models and $p(V^*_{\mathrm{rnd}})$ of the corresponding Poisson–Voronoi tessellation, see Fig. 5(b). We observe pronounced peaks in these distributions, illustrating the different environment of the generating points in CCO trees and in a purely random arrangement: The first minimum near $V=0.5\langle V\rangle$ illustrates a reduced number of smaller cells present in tree models. This result suggests some kind of repulsive effect of the tree structure on the spatial distribution of terminal end points. Likewise, the second minimum near $V=1.5\langle V\rangle$ shows a reduction in the number of larger cells in CCO trees, whereas the number of cells near the mean cell volume $V=\langle V\rangle$ is increased at the expense of smaller and larger cells. In summary, these results indicate a tendency of the tree models to more homogeneously distribute supply volumes than could be achieved by a purely random arrangement of terminal locations. Moreover, Fig. 5(b) shows that the above effects are more pronounced for CCO trees optimized for minimum segment length ($\lambda=0$) than for trees optimized for minimum intravascular volume ($\lambda=2$).

It is interesting to note that Montoro *et al.*[17] observed a similar behavior of the Voronoi cell volume distribution for certain physical conditions in their simulation study on ionic association in electrolyte solutions. The authors attributed their VP distributions to the repulsive action of Coulomb forces in the system. This further supports our notion that the repulsive effect of an existing tree on the location of new terminal sites produces differences in their spatial distribution relative to a purely random arrangement of points, and these differences are directly reflected in the properties of the respective Voronoi polyhedra.

Distribution of the Total Surface Area of the VP

Figure 6 shows the distribution of the normalized total surface area, $S^*=S/\langle S\rangle$, of the Voronoi cells. Each distribution $p(S^*)$ is fairly symmetric around its mean value. Moreover, $p(S^*)$ appears distinctly narrower for the tree models than for random points (see also the values of σ_S in Table 2). This narrowing effect in $p(S^*)$ is more pronounced for trees optimized for minimum length ($\lambda=0$) than for trees optimized for minimum volume ($\lambda=2$). In comparison to random points, the Voronoi cells of the tree models having a total surface area near the mean value $\langle S\rangle$ are favored at the expense of cells with relatively smaller and larger S. This behavior of $p(S^*)$ is consistent with the above observations of

$p(V^*)$ concerning a certain balancing effect of the growing tree structure on the spatial distribution of its terminal supply points. Based on a two-sample Kolmogorov–Smirnov test, the differences between the $p(S^*)$ distributions are statistically significant ($p<0.0001$), both between CCO models with $\lambda=2$ and $\lambda=0$ and between CCO models and random points.

Again, a two-parameter gamma distribution, Eq. (10), represents a good fit to the reference distribution $p(S^*)$ of the corresponding Poisson–Voronoi tessellation.[30] Fitting a gamma distribution to the $p(S^*)$ data of the CCO trees, also yields a fairly good approximation. Yet, there are noticeable differences between the fitted and the original distributions, in particular near their peak values. The best-fit parameters a and b are given in Table 3.

Distribution of the Asphericity Parameter

The parameter of asphericity α, Eq. (8), combines volume and surface area into a single descriptor to measure how different the shape of a polyhedron appears from that of a sphere. Figure 7 shows the distributions $p(\alpha)$ for the models studied: Markedly different from the Poisson point process, which exhibits a long asymmetric tail and has a mean value near $\alpha\approx 2$, the distributions of the CCO models are considerably narrower, more symmetric, and their mean value at $\alpha\approx 1.7$ lies close to that of a sphere ($\alpha=1$). The VP of CCO trees are thus more regular than the ones generated by a Poisson point process, again confirming the balancing effect already mentioned for VP volume and surface area distributions. In contrast to that, the differences in the $p(\alpha)$ distributions between the CCO models are only marginal: Both mean values and standard deviations are very close, only the tree for $\lambda=0$ is slightly more symmetric. However, these differences in $p(\alpha)$ are statistically significant, as are the differences between the CCO models and the random points (Kolmogorov–Smirnov test, $p<0.0001$).

DISCUSSION

Distribution of Cell Volumes

The volume of a Voronoi cell is determined by the areas A_k of its faces, by the distances r_k of its center from the corrresponding nearest neighbor points, and by the number N_f of its faces [cf. Eq. (7)]. Hence, the properties of A_k, r_k, and N_f in CCO models and in a Poisson point process provide further insight concerning the observed differences in the respective distributions of cell volumes.

Figure 8(a) shows the PDFs $d_k(r)$ of the kth nearest neighbor distances for $k=1,2,3$ for the CCO models and

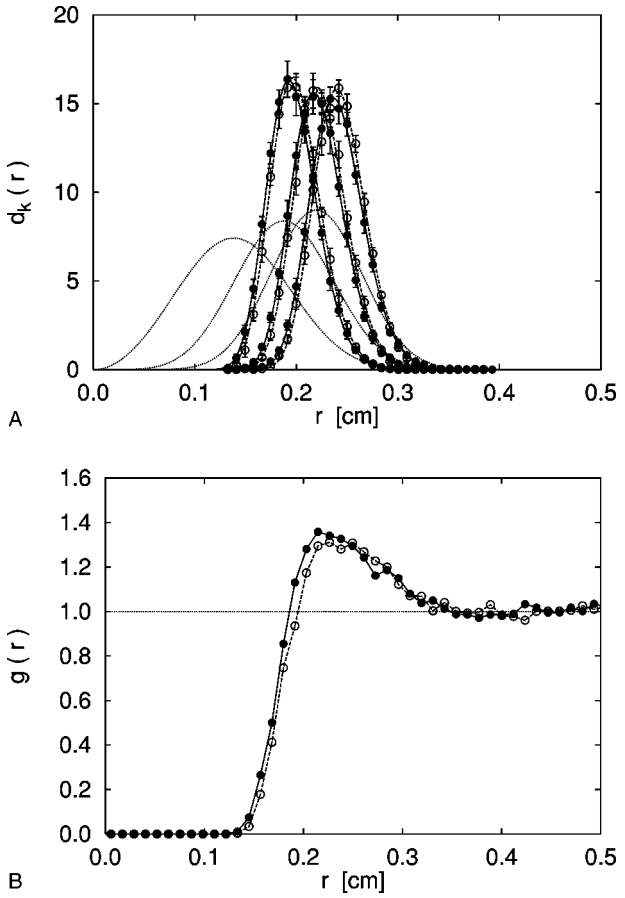

FIGURE 8. (a) Probability density distribution (mean±SD) of the *k*th nearest neighbor distances for $k=1$ (left curves), $k=2$ (middle curves), and $k=3$ (right curves) for ten realizations of CCO trees with $\lambda=2$ (solid circles with solid lines) and $\lambda=0$ (open circles with dashed lines). The dotted lines show the theoretical curves for a Poisson point process with the same density ρ, see Eq. (11). (b) Radial pair distribution functions $g(r)$ for the CCO models (symbols as earlier) and for the corresponding Poisson point process with $g(r)\equiv 1$.

for a Poisson point process with the same density of points $\rho=N/V_{\text{box}}$. For the latter, $d_k(r)$ can be written in closed form (see also Ref. 52):

$$d_k^P(r)=\rho 4\pi r^2\frac{(\rho b_r)^{k-1}}{(k-1)!}\exp(-\rho b_r), \qquad (11)$$

where $b_r=(4\pi/3)r^3$. Figure 8(a) illustrates that the first three nearest neighbor distances are always abundant in a Poisson point process relative to the CCO trees studied. Recalling that the mean number of cell faces N_f (i.e., the number of nearest neighbors for each generating point) is about 15, with maximum values ranging up to 31 (see Table 2), it is by far not sufficient to consider only the first three nearest neighbor distances to characterize their contribution to the observed cell volume distributions.

Since it is very cumbersome to analyze all nearest neighbor distances in the way given earlier, we apply the well-known concept of the (radial) pair distribution function $g(r)$.[1] This function measures the average portion of pairs of points having a distance r from each other relative to a purely random arrangement at the same density ρ. For spatially homogeneous and isotropic systems $g(r)$ can—without loss of information—be written as

$$g(r)=\frac{1}{\rho}\frac{1}{4\pi r^2}\frac{1}{N}\sum_i\sum_{j\neq i}\delta(r-r_{ij}), \tag{12}$$

where r_{ij} denotes the separation between point i and point j and $\delta(r-r_{ij})$ is the Dirac delta function. Note that in Eq. (12) any features of $g(r)$ arising from spatial inhomogeneities or anisotropies are averaged out. $g(r)$ is related to the distributions $d_k(r)$ of the kth nearest neighbor distances by

$$g(r)=\frac{1}{\rho}\frac{1}{4\pi r^2}\sum_k d_k(r). \tag{13}$$

By definition, and by means of Eqs. (11) and (13), we have $g(r)\equiv 1$ for a Poisson point process. To evaluate $g(r)$ for the CCO models, we follow the usual practice and construct a histogram of the respective pair separations.[1] The results, averaged over ten realizations of each CCO model, are shown in Fig. 8(b). We first notice a distinctive maximum in the relative frequency of pair separations around $r=0.23$ cm. This is a broad peak, indicating the contribution of many orders of neighbor separations, see Eq. (13). The greater abundance of such pair separations in CCO trees relative to random points is caused by the larger segments of the trees: since the interior of segments is excluded for new terminal positions, large (i.e., thick) segments necessarily give rise to a relatively higher frequency of pair separations near or beyond the diameter of these segments. This behavior is best recognized from the arrangement of large tree segments and neighboring Voronoi cells as shown in the 2D example of Fig. 3(a).

The low values of $g(r)$ for small r illustrate a pronounced deficiency of these pair separations in CCO trees relative to a Poisson point process. This decay is mainly due to the distribution of the first three nearest neighbor distances, see Fig. 8(a), and originates from the repulsion criterion, which suppresses small distances between new terminal locations and existing segments during tree generation.

The second important parameter characterizing the distribution of cell volumes is the area A of individual VP faces. Figure 9 shows the distribution of A grouped by selected classes of nearest neighbor separations for

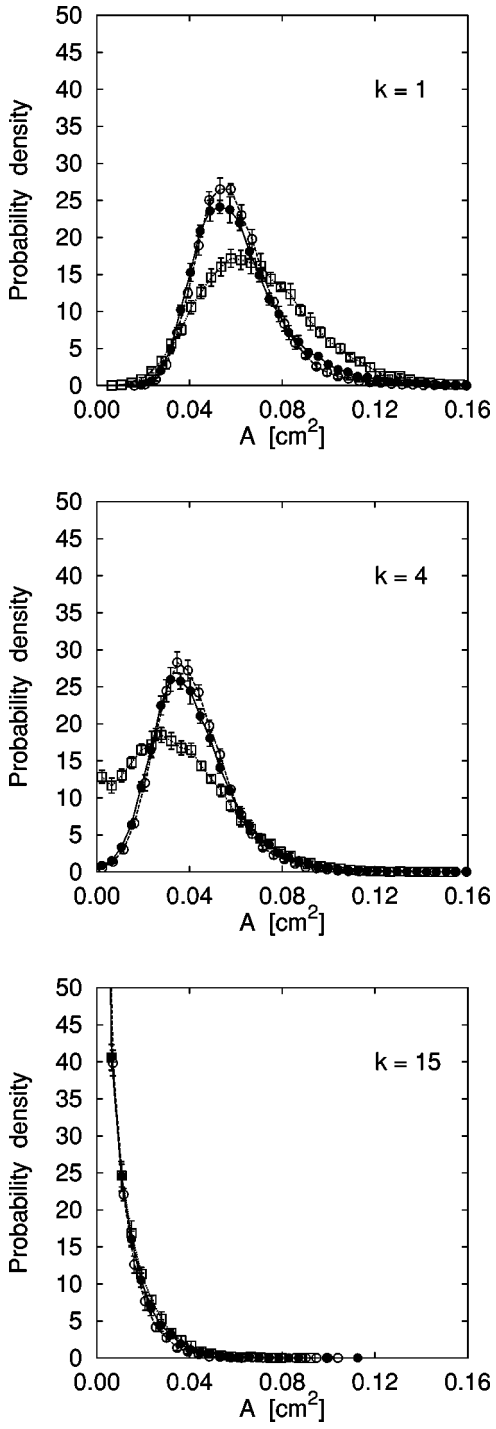

FIGURE 9. Probability density distribution (mean±SD) of the area *A* of individual polyhedra faces grouped by selected classes *k* of ascending nearest neighbor separations for which the respective faces form the perpendicular bisectors. Solid circles with solid lines: CCO trees with λ=2. Open circles with dashed lines: CCO trees with λ=0. Open squares with dotted lines: Poisson point process.

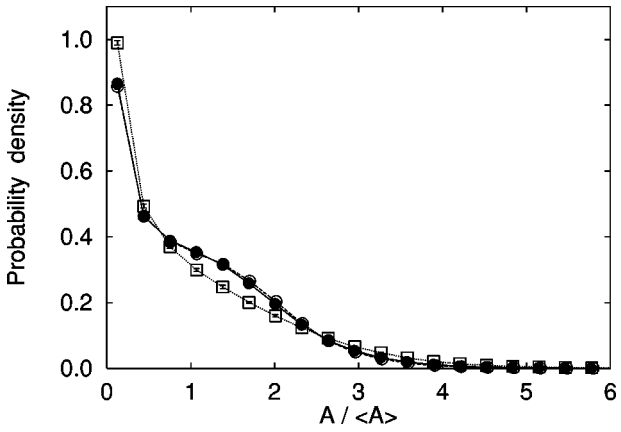

FIGURE 10. Probability density distribution (mean±SD) of the normalized area $A^*=A/\langle A\rangle$ of individual polyhedra faces. Solid circles with solid lines: CCO trees with $\lambda=2$. Open circles with dashed lines: CCO trees with $\lambda=0$. Open squares with dotted lines: Poisson point process.

which the respective faces form the perpendicular bisectors: For small A the Poisson point process always contributes with a relatively larger number of faces to V, whereas for midranged A the situation is reversed. For large A, only the face areas pertaining to the first nearest neighbors are noticeably abundant for random points in comparison with CCO trees; for higher-order neighbors, the differences between CCO trees and random points are almost negligible. These properties are consistently reflected in the overall distribution of individual face areas A, irrespective of the nearest neighbor index: Figure 10 shows the results for the distribution of $A^*=A/\langle A\rangle$. The smallest face areas and—though less pronounced—also the largest areas are favored in a Poisson point process, whereas in CCO trees face areas near the mean value appear with a relatively higher frequency. This difference in $p(A^*)$ between CCO trees and random points is confirmed by a Kolmogorov–Smirnov test ($p<0.0001$), whereas CCO models with $\lambda=2$ and $\lambda=0$ are not discriminated at the 0.0001 level of significance.

As to the third parameter which determines the distribution of V, namely the number of faces N_f per polyhedron, we first note that V and N_f are positively correlated: The correlation coefficient between N_f and V is $\rho_{N_f,V}=0.74$ for CCO models with $\lambda=2$, $\rho_{N_f,V}=0.70$ for CCO models with $\lambda=0$, and $\rho_{N_f,V}=0.65$ for random points. Figure 4 illustrates that the frequency of VP having a large number of faces $N_f>16$ (and therefore, a large cell volume) is significantly higher for random points than for CCO trees. On the contrary, VP with N_f near the mean $\langle N_f\rangle$ are found more frequently in CCO trees. For small N_f, all models behave fairly similar concerning the frequency of N_f.

In summary, the abundance of small cell volumes for random points is due to a relatively higher frequency of small pair distances [$g(r)$, see Fig. 8(b)] as well as of small individual facet areas A (Fig. 10) in these models. For intermediate cell volumes, the situation is reversed with an additional effect of N_f in favor of CCO trees. The higher frequency of larger cell volumes for random points is mainly due to A (Fig. 10) and to N_f (Fig. 4). From $g(r)$ and the distributions of A grouped by nearest neighbors (Fig. 9) it is evident, that only low-order neighbors significantly contribute to the differences in the cell volume distributions. These observations—both the distribution of nearest neighbor distances as reflected in $g(r)$ as well as the one of individual face areas together with N_f—consistently explain the differences in the distributions of Voronoi cell volumes between CCO trees and random points as displayed in Fig. 5.

Dependence of Cell Volume Statistics on the Number of End Points

For ideal (infinite) Poisson–Voronoi tessellations, the distribution $p(V^*)$ of reduced cell volumes is independent of the point density ρ due to the invariance of the generating Poisson point process under scaling.[19] However, Voronoi tessellations in a finite region of space become more and more dominated by boundary effects as the density ρ of the generating points decreases. In particular, for CCO trees it is *a priori* unclear, how cell volume statistics vary as a function of $\rho=N_{\text{term}}/V_{\text{box}}$ and if there exists a ''limiting'' distribution of cell volumes for large N_{term}. Figure 11(a) shows the $p(V^*)$ distributions for CCO models with $\lambda=2$ and with different numbers of end points ranging from $N_{\text{term}}=600$ to $N_{\text{term}}=32{,}000$. There is a modest effect of N_{term} on the respective $p(V^*)$ distributions, in particular for $N_{\text{term}}<6000$. The relative dispersions $\text{RD}_V=\sigma_V/\langle V\rangle$ tend to decrease as N_{term} increases with values between $\text{RD}_V=0.42$ for $N_{\text{term}}=600$ to $\text{RD}_V=0.36$ for $N_{\text{term}}=32{,}000$. This dependence on N_{term} is mainly due to boundary effects: excluding boundary cells from the analysis, we obtain $p(V^*)$ distributions as illustrated in Fig. 11(b). Now the variability between the distributions is considerably reduced and we find values for RD_V in the range $\text{RD}_V=0.34\pm0.01$. In summary, the chosen value of $N_{\text{term}}=6000$ for the model trees proves a reasonable compromise between the requirements for computational resources during tree generation and the validity of the reported moments of $p(V^*)$ in the limit of large N_{term}. These results suggest a certain kind of scaling invariance or self-similarity of CCO trees in the sense that ever finer tree structures reproduce properties already present at coarser levels of resolution in earlier stages of growth.

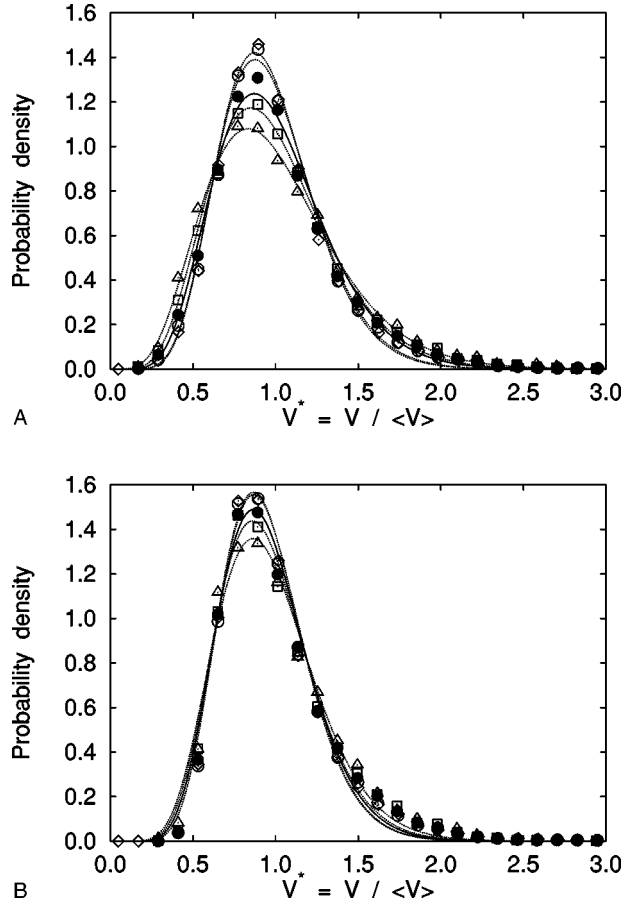

FIGURE 11. The effect of the number N_{term} of end points on the cell volume distribution. (a) Probability density distribution of the normalized cell volume $V^* = V/\langle V \rangle$ of the Voronoi polyhedra generated by CCO tree models ($\lambda = 2$) for various values of N_{term} (triangles: $N_{term} = 600$, squares: $N_{term} = 2000$, solid circles: $N_{term} = 6000$, open circles: $N_{term} = 18{,}000$, diamonds: $N_{term} = 32{,}000$). The symbols indicate mean values for 10 ($N_{term} = 600, 2000, 6000$) and 2 ($N_{term} = 18{,}000, 32{,}000$) model realizations, respectively. The dotted lines (solid line for $N_{term} = 6000$) show the corresponding best-fit two-parameter gamma distributions, Eq. (10). (b) Same as (a), boundary cells excluded from the analysis.

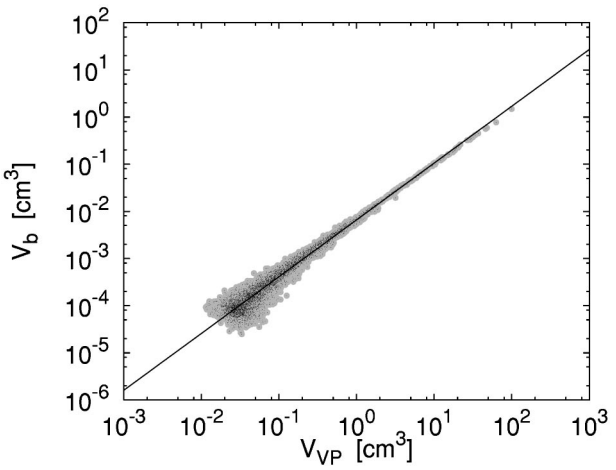

FIGURE 12. Scaling of blood volume V_b with the volume V_{VP} of supplied tissue for ten realizations of CCO trees with $\lambda = 2$ in a double-logarithmic representation. *y* axis: total intravascular volume of subtrees, excluding single terminal segments. *x* axis: total volume of Voronoi polyhedra generated by corresponding distal end points of terminal segments. The solid line is the best-fit regression to the data points.

Comparison with Experimental Data

Scaling of Blood Volume with the Volume of Supplied Tissue. Scaling relations in biology have long been a subject of discussion since their advent in the seminal work of D'Arcy Thompson.[54] Only recently, West *et al.*[60] have presented a general model for the origin of allometric scaling laws in biology, i.e., relationships of the form

$$Y = Y_0 X^s, \tag{14}$$

where Y and X are some biological observables (e.g., metabolic rate and mass of an organism), Y_0 is a normalization constant, and s the scaling exponent. Based on a few basic principles concerning the design of biological transport networks (such as a hierarchical branching structure, invariant terminal units, and minimized energy dissipation), this model predicts many scaling relations of mammalian circulatory systems, in particular a linear relationship (i.e., $s = 1$) between blood volume and total body volume in agreement with experimental data reported by Prothero.[41]

To evaluate this relation for the CCO models we consider the intravascular volume of subtrees as a function of the tissue volume supplied by each subtree. Since the Voronoi tessellation induced by the tree's terminal locations provides a convenient and unambiguous way of assigning to each terminal location a region of tissue supplied with blood, we consider—for each subtree—the total volume of the Voronoi polyhedra V_{VP} corresponding to the terminal supply points of the respective subtree. The results for the more realistic models with $\lambda = 2$ are shown in Fig. 12 in a double-logarithmic plot, where the maximum value of V_{VP} represents the whole perfusion volume. Single terminal segments (i.e., degenerated subtrees) and corresponding single polyhedra volumes have been excluded from the analysis. For the remaining data points, which still range over four orders of magnitude, a best-fit regression yields a scaling exponent of $s = 1.20 \pm 0.007$. The obvious departure of this result from the value of $s = 1$ predicted by West *et al.* is not too surprising, given the fact that we have used a constant bifurcation exponent $\gamma = 2.55$ throughout the tree and an optimization target which minimizes total intravascular volume. Both settings are different from the

assumptions and results of the model cited earlier: This model minimizes the energy dissipation of the transport network and predicts—for the more realistic case of pulsatile flow—a bifurcation exponent γ which varies from $\gamma=2$ for larger arteries to $\gamma=3$ for smaller arteries. We have also evaluated the scaling exponent s for the case $\gamma=3$. (Minimizing total intravascular volume is equivalent to energy minimization only for $\gamma=3$.)[61] Note that increasing γ in Eq. (1) slows down the rate at which segmental volumes drop along bifurcation orders and, hence, has the effect of decreasing s. Accordingly, we obtain $s=1.16\pm0.004$, a value closer to the reported value of $s=1$. This result further improves if we consider only larger subtrees: For $V_{\mathrm{VP}}>0.1$ cm^3 the value of the scaling exponent decreases to $s=1.08\pm0.005$, suggesting that CCO trees quite satisfactorily reproduce the predicted and experimentally observed scaling of blood volume with the volume of tissue supplied, provided we do not take too close a look at all the details of the smallest subunits of the model. This observation is consistent with recent results reported by Wang and Bassingthwaighte,[59] who showed that capillary supply regions, i.e., regions based on the functional measure of capillary diffusion, cannot—apart from very special cases—be approximated by Voronoi polygons; moreover, appropriate modeling of transport and consumption of oxygen in (cardiac) tissue demands a realistic geometric model for the three-dimensional nontree-like capillary network.[8] On the other hand, terminal segments of CCO trees do not represent real terminal arterioles, nor do they model capillaries, and the subdivision of tissue space into VP induced by the terminals is not based on functional considerations, but should in the present context be understood as an attempt—on purely geometric grounds—to assign to the model's terminal segments reasonable areas of blood supply.

Finally, we note that the volume of the vessels cannot be considered part of the terminal supply regions represented by the associated VP. Therefore, we have estimated—by a straight-forward Monte Carlo simulation—the portions of polyhedra volumes occupied by tree segments and corrected these volumes accordingly. For the models with $\lambda=2$ and $N_{\mathrm{term}}=6000$ the average intravascular volume is approximately 1.5 ml (i.e., only 1.5% of the total perfusion volume). Consequently, the effects of tree volume are only marginal: Neither the distribution of Voronoi cell volumes nor the scaling of blood volume with (now corrected) supply volume are noticeably different from the uncorrected case.

Scaling of Arterial Cross-Sectional Area with the Volume of Supplied Tissue. Seiler *et al.*[51] have reported a power-law relationship between luminal cross-sectional area a of human coronary artery segments and perfused regional myocardial mass

$$a \propto V_{\mathrm{VP}}^{\beta}, \tag{15}$$

with exponents β in the range between 0.62 and 0.82. In good agreement with these results we find for the models with $\lambda=2$ a scaling exponent of $\beta=0.77\pm0.01$ (Fig. 13), where terminal segments and associated single polyhedra volumes have again been excluded from the regression analysis.

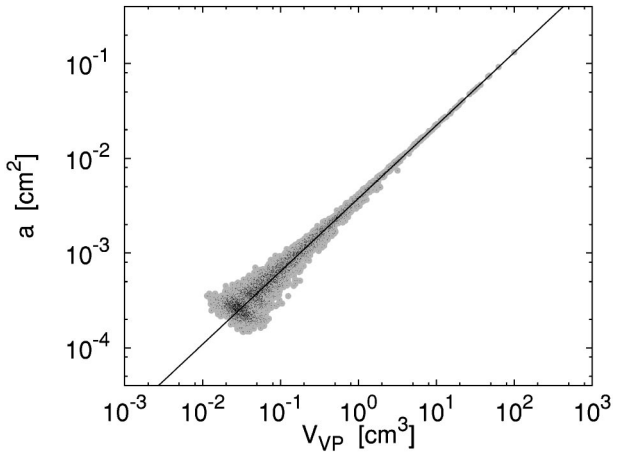

FIGURE 13. Scaling of segmental cross-sectional area *a* (terminals excluded) with the volume V_{VP} of tissue supplied by the respective subtrees for ten realizations of CCO models with $\lambda=2$. The solid line represents the least-squares fit of a power-law relation, Eq. (15), to the data points.

Voronoi Cell Area Distribution of Arterial End Points in the Human Retina. Two-dimensional CCO models are convenient for a comparison of Voronoi cell area distributions with physical data. Here, we attempt a comparison with the major arteries of the approximately two-dimensional layer of the human retina. From data published by Zamir *et al.*,[63] we digitized just visible arterial end points within a square region of about 5 mm sidelength centered around the macular area, using the original fundus photograph (their Fig. 1) and a map of major retinal vessels (their Fig. 2). The resulting set of apparent end points and its Voronoi tessellation are shown in Fig. 14(a). In order to provide comparable model data, we have pruned the model trees to the same number of terminal segments as points digitized. Figure 14(b) shows the distributions of normalized Voronoi cell areas of the experimental data and pruned 2D CCO trees with original $N_{\mathrm{term}}=3000$ and $\lambda=2$. In both cases, boundary cells were excluded from the analysis to reduce edge effects. The model distribution appears in good

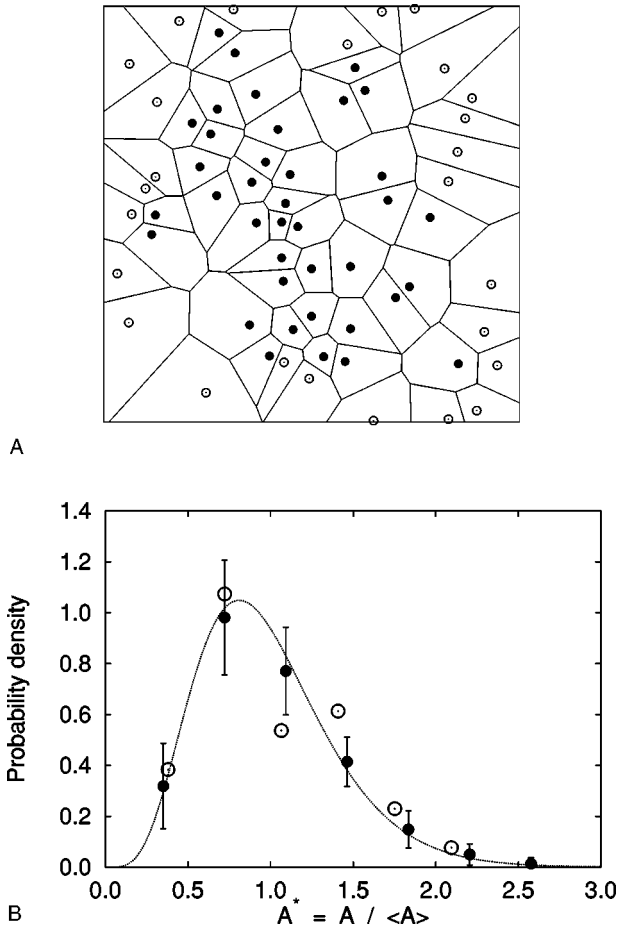

FIGURE 14. (a) Voronoi tessellation of apparent arterial end points digitized from data of the human retina published by Zamir *et al.* (Ref. 63). (b) Probability density distribution (mean±SD) of normalized Voronoi cell area $A^*=A/\langle A\rangle$ generated by ten realizations of pruned 2D CCO trees (solid circles) and by the points of panel (a) (open circles). The continuous line shows the best-fit two-parameter gamma distribution for the model trees.

qualitative agreement with the measured data. However, due to the difficulties in identifying segmental end points in the retinal fundus photograph, the results shown in Fig. 14 currently do not allow a quantitative assessment of model predictions regarding the spatial distribution of end points in the retinal arterial system.

A Modified Algorithm for Tree Construction

In the previous section we have used the Voronoi polyhedra associated with individual terminal segments as a geometric model for the regions of tissue supplied by these segments. The reported scaling properties illustrate that this model is a reasonable approach within the framework of CCO trees.

These observations suggest a modification of the present method of CCO, namely to set terminal flows proportional to their associated Voronoi cell volumes after each step of growth and to rescale segment diameters of the whole tree accordingly to meet the modified boundary conditions. This approach is further supported by a recent paper of Qian and Bassingthwaighte,[42] who showed that asymmetric branching tree models with random flow variations at each bifurcation give rise to an asymptotic lognormal flow distribution, in favorable agreement with experimental measurements of regional blood flow distributions in the heart and lung. (Note that we have used two-parameter gamma distributions to characterize Voronoi cell volumes in CCO trees; however, Vaz and Fortes[57] have shown that two-parameter gamma and lognormal distributions with suitable parameters are very similar.)

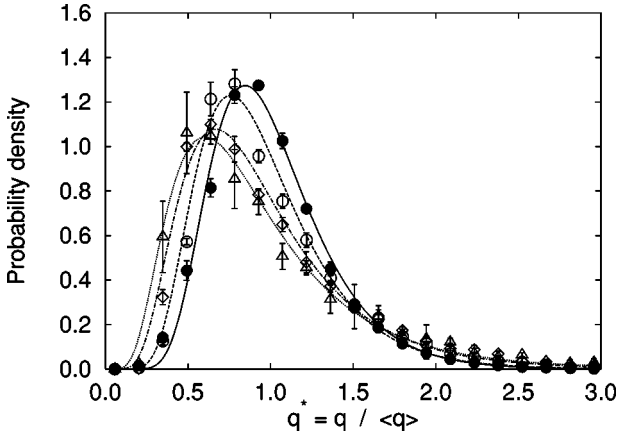

FIGURE 15. Probability density distribution (mean±SD) of normalized segmental flows $q^*=q/\langle q\rangle$ for three realizations of CCO tree models ($\lambda=2$) grown by the modified algorithm. Data are grouped by Strahler orders i_S of the respective segments. The continuous lines show best-fit lognormal distributions, Eq. (16). $i_S=1$ (terminals): solid circles and solid line. $i_S=2$ (preterminals): open circles and dashed line. $i_S=3$: diamonds and dashed-dotted line. $i_S=4$: triangles and dotted line.

Figure 15 shows the distributions of normalized segmental flows, $q^*=q/\langle q\rangle$, for CCO trees ($\lambda=2$) grown by the modified algorithm and with other model parameters left unchanged (Table 1). The data are grouped by Strahler orders[53] of the respective segments and approximated by best-fit lognormal distributions

$$p(x)=\frac{1}{\sqrt{2\pi}x\log\sigma_g}\exp\left[-\frac{(\log x-\log\langle x\rangle_{0.5})^2}{2\log^2\sigma_g}\right],\quad x>0, \tag{16}$$

where $\langle x\rangle_{0.5}$ is the median and σ_g is the geometric standard deviation. [Qian and Bassingthwaighte[42] considered flow distributions as a function of generation numbers in strictly dichotomous binary trees; for the asymmetric topology of CCO trees the Strahler ordering scheme seems more appropriate: terminal segments are assigned order

1; if two first-order segments meet, the parent (i.e., preterminal) segment is assigned order 2, and so forth.] Figure 15 illustrates that the distribution $p(q^*)$ of normalized terminal flows is well approximated by a lognormal distribution, and this property is approximately also observed for higher-order segments, consistent with the results of Ref. 42. For the terminal flows we find a relative dispersion of $RD_q = 37\%$ and a skewness coefficient of $\gamma_q = 1.12$. Both values are in good agreement with data reported for experimental measurements of regional blood flow in the heart and the lung.[6,14] Moreover, RD_q and γ_q are roughly independent on the number N_{term} of terminal segments (see the previous discussion on N_{term} dependence), suggesting that these values represent an invariant property of CCO tree models, at least for the parameter space considered in the present work.

We finally note that the modified algorithm has no significant effect on other characteristics of the model, e.g., the distribution of segment diameters and VP volumes, the pressure profile, the total tree volume, and the distribution of segments over Strahler orders.

SUMMARY AND CONCLUSIONS

In this paper we have analyzed topological and metric properties of the Voronoi polyhedra generated by the distal end points of terminal segments in CCO trees and by randomly distributed points as a reference model with the aim to characterize the spatial distribution of the respective point sets.

We have evaluated the distributions of the number N_f of Voronoi cell faces, the cell volume V, surface area S, the area A of individual cell faces, and the asphericity parameter α. We have characterized the distributions of these quantities by their respective moments and by approximation with best-fit two-parameter gamma distributions (Tables 2 and 3). The distributions of N_f, V, S, A, and α of the CCO models all proved significantly different from the ones obtained for the random points, whereas the distributions of V, S, and α were also significantly different between CCO models generated with different modes of optimization (two-sample Kolmogorov–Smirnov test, $p < 0.0001$). Two-parameter gamma distributions not only characterize the distributions of N_f, V, and S for Poisson–Voronoi tessellations,[30] but also provide a reasonable approximation for the distributions of these quantities in CCO models.

Both the distribution of Voronoi cell volumes and the distribution of kth nearest neighbor distances as reflected in the pair distribution function $g(r)$ consistently showed the repulsive effect of a growing CCO tree structure on the spatial arrangement of its terminal supply points as well as the tendency of such trees to balance the cell volume distribution observed for random points: CCO trees increase the number of Voronoi cells having volumes near the mean value $\langle V \rangle$ at the expense of small and large cells, i.e., the cell volume distribution for CCO models is more homogeneous than for random points.

For comparison of model predictions with experimental data we have studied scaling of intravascular blood volume and of arterial cross-sectional area with the volume of supplied tissue, which we have modeled on a geometrical (not functional) basis by the VP generated by the model's terminal segments. Depending on the particular value of the bifurcation exponent γ and on the size of subtrees considered, we have found scaling exponents between $s = 1.20 \pm 0.007$ and $s = 1.08 \pm 0.005$ for intravascular blood volume and $\beta = 0.77 \pm 0.01$ for arterial cross-sectional area. These results are consistent with experimental data and model predictions reported in the literature.[41,51,60]

Based on these observations we have extended the CCO algorithm to set terminal flows proportional to associated VP volumes. As a major improvement of the model we now obtain terminal flows well approximated by a lognormal distribution with a relative dispersion of $RD_q = 37\%$ and a skewness coefficient of $\gamma_q = 1.12$, in good agreement with theoretical considerations[42] and experimental measurements of regional blood flow distributions.[6,14]

The first conclusion we draw from this study is that Voronoi analysis proved a valuable tool to characterize the spatial distribution of end points governed by the presence of a growing CCO tree structure and to discriminate such distributions from a purely random arrangement of points. From the comparison of model predictions with experimentally observed scaling properties of intravascular blood volume and arterial cross-sectional area with supplied tissue volume we conclude that assigning to each terminal segment its corresponding Voronoi polyhedron reasonably defines the regions of tissue supplied by individual terminal segments in CCO trees. Finally, a modified algorithm of tree construction with terminal flows set proportional to Voronoi volumes yields a considerable improvement of the model, in particular with respect to the distribution of terminal flows. For future developments, this new mode of tree generation may prove useful to study flow heterogeneity within the framework of CCO trees.

ACKNOWLEDGMENTS

The authors gratefully acknowledge the valuable advice from the editor regarding the literature and the critical comments provided by the anonymous reviewers of this study.

REFERENCES

[1] Allen, M. P., and D. J. Tildesley. Computer Simulation of Liquids. Oxford: Oxford University Press, 1987, pp. 54–55.

[2] Arts, T., R. T. I. Kruger, W. VanGerven, J. A. C. Lambregts, and R. S. Reneman. Propagation velocity and reflection of pressure waves in the canine coronary artery. *Am. J. Physiol.* 237:H469–H474, 1979.

[3] Aurenhammer, F., and R. Klein. Voronoi diagrams. In: Handbook of Computational Geometry, edited by J. R. Sack and J. Urrutia. Amsterdam: Elsevier Science B. V., 2000, pp. 201–290.

[4] Barber, C. B., and H. Huhdanpaa. Qhull version 2.6. The Geometry Center, University of Minnesota, Minneapolis, 1998. http://www.geom.umn.edu/locate/qhull.

[5] Barber, C. B., D. P. Dobkin, and H. Huhdanpaa. The quickhull algorithm for convex hulls. *ACM Trans. Math. Softw.* 22:469–483, 1996.

[6] Bassingthwaighte, J. B., R. B. King, and S. A. Roger. Fractal nature of regional myocardial blood flow heterogeneity. *Circ. Res.* 65:578–590, 1989.

[7] Beard, D. A., and J. B. Bassingthwaighte. The fractal nature of myocardial blood flow emerges from a whole-organ model of arterial network. *J. Vasc. Res.* 37:282–296, 2000.

[8] Beard, D. A., and J. B. Bassingthwaighte. Modeling advection and diffusion of oxygen in complex vascular networks. *Ann. Biomed. Eng.* 29:298–310, 2001.

[9] Brown, D. Voronoi diagrams from convex hulls. *Inf. Process. Lett.* 9:223–228, 1979.

[10] Chilian, W. M., S. M. Layne, E. C. Klausner, C. L. Eastham, and M. L. Marcus. Redistribution of coronary microvascular resistance produced by dipyridamole. *Am. J. Physiol.* 256:H383–H390, 1989.

[11] Chilian, W. M. Microvascular pressures and resistances in the left ventricular subepicardium and subendocardium. *Circ. Res.* 69:561–570, 1991.

[12] Dirichlet, G. L. Uber die Reduction der positiven quadratischen Formen mit drei unbestimmten ganzen Zahlen. *J. Reine Angew. Math.* 40:209–227, 1850.

[13] Fung, Y. C. Biomechanics: Motion, Flow, Stress, and Growth. New York: Springer, 1990, pp. 155–195.

[14] Glenny, R. W., and H. T. Robertson. Fractal properties of pulmonary blood flow: Characterization of spatial heterogeneity. *J. Appl. Physiol.* 69:532–545, 1990.

[15] Glenny, R. W., and H. T. Robertson. A computer simulation of pulmonary perfusion in three dimensions. *J. Appl. Physiol.* 79:357–369, 1995.

[16] Gil Montoro, J. C., and J. L. F. Abascal. The Voronoi polyhedra as tools for structure determination in simple disordered systems. *J. Phys. Chem.* 97:4211–4215, 1993.

[17] Gil Montoro, J. C., F. Bresme, and J. L. F. Abascal. Ionic association in electrolyte solutions: A Voronoi polyhedra analysis. *J. Chem. Phys.* 101:10892–10898, 1994.

[18] Gödde, R., and H. Kurz. Structural and biophysical simulation of angiogenesis and vascular remodeling. *Dev. Dyn.* 220:387–401, 2001.

[19] Hinde, A. L., and R. E. Miles. Monte Carlo estimates of the distributions of the random polygons of the Voronoi tessellation with respect to a Poisson process. *J. Stat. Comput. Simul.* 10:205–223, 1980.

[20] Honda, H. Description of cellular patterns by Dirichlet domains: The two-dimensional case. *J. Theor. Biol.* 72:523–543, 1978.

[21] Hoofd, L., Z. Turek, K. Kubat, B. E. M. Ringnalda, and S. Kazda. Variability of intercapillary distance estimated on histological sections of rat heart. *Adv. Exp. Med. Biol.* 191:239–247, 1985.

[22] Hudlicka, O., A. J. Wright, and A. M. Ziada. Angiogenesis in the heart and skeletal muscle. *Can. J. Cardiol.* 2:120–123, 1986.

[23] Jedlovszky, P. Voronoi polyhedra analysis of the local structure of water from ambient to supercritical conditions. *J. Chem. Phys.* 111:5975–5985, 1999.

[24] Kamiya, A., and T. Togawa. Optimal branching structure of the vascular tree. *Bull. Math. Biophys.* 34:431–438, 1972.

[25] Karch, R., F. Neumann, M. Neumann, and W. Schreiner. A three-dimensional model for arterial tree representation, generated by constrained constructive optimization. *Comput. Biol. Med.* 29:19–38, 1999.

[26] Karch, R., F. Neumann, M. Neumann, and W. Schreiner. Staged growth of optimized arterial model trees. *Ann. Biomed. Eng.* 28:495–511, 2000.

[27] Kassab, G. S., C. A. Rider, N. J. Tang, and Y.-C. B. Fung. Morphometry of pig coronary arterial trees. *Am. J. Physiol.* 265:H350–H365, 1993.

[28] Kassab, G. S., J. Berkley, and Y. C. B. Fung. Analysis of pig's coronary arterial blood flow with detailed anatomical data. *Ann. Biomed. Eng.* 25:204–217, 1997.

[29] King, R. B., L. J. Weissman, and J. B. Bassingthwaighte. Fractal descriptions for spatial statistics. *Ann. Biomed. Eng.* 18:111–121, 1980.

[30] Kumar, S., S. K. Kurtz, J. R. Banavar, and M. G. Sharma. Properties of a three-dimensional Poisson–Voronoi tesselation: A Monte Carlo study. *J. Stat. Phys.* 67:523–551, 1992.

[31] Kumar, S., and S. K. Kurtz. Properties of a two-dimensional Poisson–Voronoi tesselation: A Monte-Carlo study. *Mater. Charact.* 31:55–68, 1993.

[32] Kurz, H., and K. Sandau. Modelling of blood vessel development. Bifurcation pattern and hemodynamics, optimality and allometry. *Comments Theor. Biol.* 4:261–291, 1997.

[33] Levy, S., T. Munzer, M. Phillips, C. Fowler, N. Thurston, D. Krech, S. Wisdom, D. Meyer, and T. Rowley. Geomview version 1.6.1. The Geometry Center, University of Minnesota, Minneapolis, 1998. http://www.geomview.org.

[34] Lipowsky, H. H., and B. W. Zweifach. Methods for the simultaneous measurement of pressure differentials and flows in single unbranched vessels of the microcirculation for rheological studies. *Microvasc. Res.* 14:345–361, 1977.

[35] Meijering, J. L. Interface area, edge length, and number of vertices in crystal aggregates with random nucleation. *Philips Res. Rep.* 8:270–290, 1953.

[36] Murray, C. D. The physiological principle of minimum work. I. The vascular system and the cost of blood volume. *Proc. Natl. Acad. Sci. U.S.A.* 12:207–214, 1926.

[37] Neumann, M., F. J. Vesely, O. Steinhauser, and P. Schuster. Solvation of large dipoles. I. A molecular dynamics study. *Mol. Phys.* 35:841–855, 1978.

[38] Neumann, F., M. Neumann, R. Karch, and W. Schreiner. Visualization of computer-generated arterial model trees. In: Simulation Modelling in Bioengineering, edited by M. Cerrolaza, D. Jugo, and C. A. Brebbia. Southampton: Computational Mechanics, 1996, pp. 259–268.

[39] Okabe, A., B. Boots, K. Sugihara, and S. N. Chiu. Spatial Tessellations: Concepts and Applications of Voronoi Diagrams, Second Edition. Chichester: Wiley, 1999.

[40] Preparata, F. P., and M. I. Shamos. Computational Geometry. An Introduction. New York: Springer, 1985.

[41] Prothero, J. W. Scaling of blood parameters in mammals. *Comparative Biochem. Physiol.* 67A:649–657, 1980.

[42] Qian, H., and J. B. Bassingthwaighte. A class of flow bifur-

cation models with lognormal distribution and fractal dispersion. *J. Theor. Biol.* 205:261–268, 2000.
[43] Rahman, A. Liquid structure and self-diffusion. *J. Chem. Phys.* 45:2584–2592, 1966.
[44] Ripley, B. D. Test of 'randomness' for spatial point patterns. *J. R. Statist. Soc. B* 41:368–374, 1979.
[45] Rosen, R. Optimality Principles in Biology. London: Butterworth, 1967, pp. 40–60.
[46] Ruocco, G., M. Sampoli, and R. Vallauri. Analysis of the network topology in liquid water and hydrogen sulphide by computer simulation. *J. Chem. Phys.* 96:6167–6176, 1992.
[47] Sandau, K., and H. Kurz. Modelling of vascular growth processes: A stochastic biophysical approach to embryonic angiogenesis. *J. Microsc.* 175:205–213, 1994.
[48] Schreiner, W. Computer generation of complex arterial tree models. *J. Biomed. Eng.* 15:148–149, 1993.
[49] Schreiner, W., and P. Buxbaum. Computer-optimization of vascular trees. *IEEE Trans. Biomed. Eng.* 40:482–491, 1993.
[50] Schreiner, W., M. Neumann, F. Neumann, S. M. Roedler, A. End, P. Buxbaum, M. R. Müller, and P. Spieckermann. The branching angles in computer-generated optimized models of arterial trees. *J. Gen. Physiol.* 103:975–989, 1994.
[51] Seiler, C., R. L. Kirkeeide, and K. L. Gould. Basic structure-function relations of the epicardial coronary vascular tree. *Circulation* 85:1987–2003, 1992.
[52] Stoyan, D., and H. Stoyan. Fractals, Random Shapes and Point Fields. Chichester: Wiley, 1994.
[53] Strahler, A. N. Quantitative analysis of watershed geomorphology. *Trans. Am. Geophys. Union* 38:913–920, 1957.
[54] Thompson, D. W. On Growth and Form. Cambridge, MA: Cambridge University Press, 1917.
[55] Van Bavel, E., and J. A. E. Spaan. Branching patterns in the porcine coronary arterial tree. Estimation of flow heterogeneity. *Circ. Res.* 71:1200–1212, 1992.
[56] Van Beek, J. H. G. M., S. A. Roger, and J. B. Bassingthwaighte. Regional myocardial flow heterogeneity explained with fractal networks. *Am. J. Physiol.* 257:H1670–H1680, 1989.
[57] Vaz, M. F., and M. A. Fortes. Grain size distribution: The lognormal and the gamma distribution functions. *Scr. Metall.* 22:35–40, 1988.
[58] Voronoi, G. Nouvelles applications des parametres continus a la theorie des formes quadratiques. *J. Reine Angew. Math.* 134:198–287, 1908.
[59] Wang, C. Y., and J. B. Bassingthwaighte. Capillary supply regions. *Math. Biosci.* 173:103–114, 2001.
[60] West, G. B., J. H. Brown, and B. J. Enquist. A general model for the origin of allometric scaling laws in biology. *Science* 276:122–126, 1997.
[61] Woldenberg, M. J., and K. Horsfield. Relation of branching angles to optimality for four cost principles. *J. Theor. Biol.* 122:187–204, 1986.
[62] Zamir, M. Optimality principles in arterial branching. *J. Theor. Biol.* 62:227–251, 1976.
[63] Zamir, M., J. A. Medeiros, and T. K. Cunningham. Arterial bifurcations in the human retina. *J. Gen. Physiol.* 74:537–548, 1979.